

UNIONS-3500 Weak Lensing: III. *B*-mode validation for cosmic shear

C. Daley¹ ^{*}, A. Guinot², S. Guerrini³, F. Hervas-Peters¹, L. W. K. Goh^{4,5}, C. Murray¹, M. Kilbinger¹, A. Wittje⁶, H. Hildebrandt⁶, M. J. Hudson^{7,8,9}, L. van Waerbeke¹⁰, T. de Boer¹¹, E. Magnier¹¹, and others

¹ Université Paris-Saclay, Université Paris Cité, CEA, CNRS, AIM, F-91191 Gif-sur-Yvette, France

² Department of Physics, McWilliams Center for Cosmology, Carnegie Mellon University, Pittsburgh, PA 15213, USA

³ Université Paris Cité, Université Paris-Saclay, CEA, CNRS, AIM, F-91191 Gif-sur-Yvette, France

⁴ Institute for Astronomy, University of Edinburgh, Royal Observatory, Blackford Hill, Edinburgh EH9 3HJ, UK

⁵ Higgs Centre for Theoretical Physics, School of Physics and Astronomy, The University of Edinburgh, Edinburgh EH9 3FD, UK

⁶ Ruhr University Bochum, Faculty of Physics and Astronomy, Astronomical Institute (AIRUB), German Centre for Cosmological Lensing, 44780 Bochum, Germany

⁷ Department of Physics and Astronomy, University of Waterloo, 200 University Avenue West, Waterloo, Ontario N2L 3G1, Canada

⁸ Waterloo Centre for Astrophysics, University of Waterloo, Waterloo, Ontario N2L 3G1, Canada

⁹ Perimeter Institute for Theoretical Physics, 31 Caroline St. North, Waterloo, ON N2L 2Y5, Canada

¹⁰ Department of Physics and Astronomy, University of British Columbia, 6224 Agricultural Road, V6T 1Z1, Vancouver, Canada

¹¹ Institute for Astronomy, University of Hawaii, 2680 Woodlawn Drive, Honolulu HI 96822, USA

Received XXXX; accepted YYYY

ABSTRACT

At Stage-III sensitivities, cosmic shear *B* modes unambiguously indicate systematic contamination and are often used to inform data selection and scale cuts for cosmological inference. We present *B*-mode validation for the UNIONS weak-lensing survey using three complementary *E/B* statistics to establish data-driven scale cuts. We compute pure-mode correlation functions $\xi_{\pm}^{E/B}(\theta)$, COSEBI *B*-mode amplitudes B_n , and harmonic-space angular power spectra C_{ℓ}^{BB} on four UNIONS catalog versions spanning $2517 \text{ deg}^2 - 2894 \text{ deg}^2$ with effective source densities 5.0 arcmin^{-2} to 6.5 arcmin^{-2} . *B*-mode detections and blinded-inference null-test failures prompted us to examine size cuts and stellar halo masking. For each statistic, we compute probability-to-exceed (PTE) over a two-dimensional grid of scale-cut boundaries; the adopted cuts lie in stable high-PTE regions and are not fine-tuned. Leakage-corrected measurements show minimal *B*-mode contamination across three statistical frameworks after scale cuts: pure-mode PTEs of 0.30 (ξ_+^B) and 0.27 (ξ_-^B), COSEBI PTE of 0.78, and harmonic-space PTE of 0.39 all pass the 0.05 threshold. Pure-mode and COSEBI diagnostics both support 12–83 arcmin scale cuts for ξ_+ and ξ_- , while harmonic-space *B* modes appear at $\ell < 300$ and $\ell \gtrsim 1600$. A persistent approximately 10 arcmin excess in ξ_+^B coinciding with the MegaCam CCD angular scale remains unresolved. Scale cuts reduce *B*-mode power to levels consistent with zero contamination across all three statistics. Multi-statistic cross-validation identifies systematic patterns invisible to any single framework—an approach that applies directly to Stage-IV surveys where systematic errors are expected to dominate statistical uncertainties.

Key words. Cosmology – weak lensing – gravitational lensing – methods: statistical

1. Introduction

Weak gravitational lensing distorts the observed shapes of distant galaxies, encoding information about the intervening matter distribution along the line of sight (Blandford et al. 1991; Miralda-Escude 1991; Kaiser 1992). First detections came in 2000 (Bacon et al. 2000; Kaiser et al. 2000; Van Waerbeke et al. 2000; Wittman et al. 2000). The scalar gravitational potential produces a shear field that is curl-free to leading order and can be decomposed into gradient-like *E* modes and curl-like *B* modes; scalar density perturbations generate *E*-mode power to leading order (Stebbins 1996; Kamionkowski et al. 1997). Higher-order effects (lens-lens coupling, source clustering, and intrinsic alignments) can produce *B*-mode contributions (Hilbert et al. 2009; Schneider et al. 2002; Crittenden et al. 2002), but these are orders of magnitude below current sensitivity—a detection challenge even for Stage-IV surveys (Schneider et al. 2022). For

galaxy shear measurements at current sensitivity, detected *B*-mode power indicates residual observational systematic effects rather than cosmological signal, though the absence of *B* modes does not guarantee freedom from systematic effects.

Stage-III cosmic shear surveys constrained the structure growth parameter $S_8 \equiv \sigma_8 \sqrt{\Omega_m}/0.3$ to per cent level precision. KiDS-1000 (Asgari et al. 2021), DES Y3 (Abbott et al. 2022), and HSC Y3 (Li et al. 2023) achieved 2–4 per cent constraints, comparable to the approximately 2 per cent uncertainty from Planck Collaboration (2020). Earlier Stage-III analyses showed persistent tension with *Planck*, with KiDS-1000 reporting approximately 3σ disagreement, but more recently KiDS-Legacy (Wright et al. 2025) found $S_8 = 0.815^{+0.016}_{-0.021}$ in only 0.73σ disagreement with *Planck*. Stage-IV surveys will reduce statistical uncertainties further, shifting the error budget toward systematic effects. Validating these methods on Stage-III data is therefore essential before analyses become systematics-limited.

^{*} e-mail: cail.daley@cea.fr

B-mode statistics are valuable for identifying systematic contamination in recent surveys. Early COSEBI (Complete Orthogonal Sets of *E/B*-mode Integrals; Section 3) analyses of CFHTLenS, DES-SV, and KiDS-450 detected significant *B* modes at 2–5 σ (Asgari et al. 2019); CFHTLenS and KiDS-450 showed signatures consistent with repeating additive shear bias (a detector-level shear offset, fixed in focal-plane coordinates, that stamps the same pattern onto each survey pointing), while DES-SV exhibited a superposition of multiple systematics including PSF leakage and photometric selection effects. HSC Y3 identified significant *B* modes in both configuration and harmonic space ($\theta > 60'$, $\ell < 300$; Li et al. 2023; Dalal et al. 2023), with follow-up analysis attributing the large-scale contamination to PSF fourth-moment leakage (Zhang et al. 2023). DES Y1 and Y3 passed *B*-mode null tests for the primary metacalibration catalogs (Asgari & Heymans 2019; Gatti et al. 2021), though the Y1 IM3SHAPE catalog exhibited the oscillatory *B*-mode signature characteristic of repeating additive shear bias. Different systematics produce distinct COSEBI mode patterns: PSF leakage, photometric selection effects, and field-of-view-scale additive offsets each generate recognizable signatures, making COSEBIs diagnostic as well as sensitive (Asgari et al. 2019). A recent uniform reanalysis found that DES-Y3 and HSC-Y3 fail *B*-mode tests when using the Hybrid-*E/B* method, though with negligible impact on cosmological constraints (Jefferson et al. 2025). KiDS-Legacy initially failed *B*-mode null tests; investigation traced the excess to astrometric systematic effects, which conservative masking then eliminated with negligible impact on S_8 constraints (Wright et al. 2025). *B*-mode statistics are therefore useful for identifying systematics and setting scale cuts, though detected contamination does not always propagate to cosmological parameters. Conversely, passing *B*-mode null tests does not rule out all systematic contamination; multiplicative shear calibration errors, for example, bias *E*-mode power without producing detectable *B* modes (Schneider et al. 2022).

Several methods separate *E*- and *B*-mode contributions in shear two-point statistics. Aperture mass dispersion (Schneider 1996; Schneider et al. 1998) is the foundational real-space method for clean *E/B* separation, though correlation functions must extend to zero separation, which complicates practical implementation. COSEBIs (Schneider et al. 2010; Asgari et al. 2012) generalize this approach, compressing all *E/B*-separable information from $\xi_{\pm}(\theta)$ on a finite angular interval into discrete orthogonal modes. A small number of modes captures the cosmological signal; by construction, the COSEBI basis excludes the ambiguous modes that cannot be assigned pure *E* or *B* character on a finite interval. Pure-mode correlation functions $\xi_{\pm}^{E/B}(\theta)$ (Schneider et al. 2022) are an alternative real-space representation that decomposes ξ_{\pm} into *E*-mode, *B*-mode, and ambiguous components through integral transforms derived from the COSEBI basis functions. Harmonic-space pseudo- C_{ℓ} estimators measure C_{ℓ}^{EE} and C_{ℓ}^{BB} directly but require careful treatment of mask-induced *E/B* mixing. We compare all three to test for method-dependent systematics and confirm consistency.

The Ultraviolet Near-Infrared Optical Northern Survey (UNIONS; Gwyn et al. 2025) combines multi-band imaging from telescopes in Hawai'i over approximately 4600 deg 2 of northern sky: the Canada-France Imaging Survey (CFIS) contributes *u*- and *r*-band from CFHT, Pan-STARRS contributes *i*- and *z*-band, and Subaru adds *z*-band imaging through WISHES and *g*-band through WHIGS. UNIONS is the primary ground-based optical complement to the *Euclid* space mission. Shape measurements are derived from CFIS *r*-band exposures using the ShapePipe pipeline (Farrens et al. 2022; Guinot et al. 2022);

catalog properties are detailed in Section 2. We present *B*-mode validation tests for the first UNIONS cosmic shear cosmology analysis using three complementary statistics: pure-mode correlation functions $\xi_{\pm}^{E/B}(\theta)$, COSEBIs, and harmonic-space power spectra C_{ℓ}^{BB} . We use measurements of $\xi_{\pm}^{B}(\theta)$ to define angular scale cuts within a blinded analysis framework. Because pure-mode correlation functions localize to specific angular scales, they are well suited for data-driven scale selection. We test the robustness of adopted cuts; their impact on cosmological constraints is evaluated in Papers IV and V.

This paper is one of five coordinated UNIONS weak-lensing publications: catalog construction (Paper I; Hervas Peters et al. 2025a), simulations and validation (Paper II; Hervas Peters et al. 2025b), the present *B*-mode validation (Paper III), configuration-space cosmological constraints (Paper IV; Goh et al. 2025), and harmonic-space cosmological constraints (Paper V; Guerrini et al. 2025). Section 2 describes the UNIONS shear catalogs and their evolution. Section 3 details the three *E/B*-separable statistics and covariance framework. Section 4 presents measurements and PTE assessments. Section 5 discusses systematic trends and methodological implications.

2. Data

UNIONS (Gwyn et al. 2025) is the largest deep weak-lensing survey of the northern sky, with photometric depth comparable to the first year of the Legacy Survey of Space and Time (LSST). The UNIONS shape measurements are derived from CFIS *r*-band exposures using the ShapePipe pipeline (Farrens et al. 2022; Guinot et al. 2022); full catalog construction is described in Paper I. The *r*-band reaches $r \approx 24.5$ at 10 σ depth with 0.7 median seeing.

We analyze four variants of the ShapePipe v1.4 catalog (Paper I, Table 2). The initial catalog (v1.4.5) applies a loose size cut ($r_{h,\text{gal}}/r_{h,\text{psf}} > 0.5$). The size-cut variant (v1.4.6.3) tightens this threshold to $r_{h,\text{gal}}/r_{h,\text{psf}} > 0.707$, removing galaxies where shape measurement and leakage correction are least reliable. The masked variant (v1.4.8) retains the v1.4.6.3 size cut and adds bright-star ($r < 12$) and faint-star ($12 < r < 18$) halo masking, reducing sky coverage by ≈ 13 per cent. The relaxed-flags variant (v1.4.11.3) reverts to the v1.4.6.3 footprint and relaxes the SExtractor flags criterion to include deblended objects, increasing the effective galaxy density by 23 per cent (Paper I). We introduced these refinements after blinded validation tests showed early signs of systematic contamination (Paper I). We adopt v1.4.6.3 as the fiducial for *B*-mode validation; Papers IV and V use the same fiducial.

For each catalog version, shear measurements are available both with and without an object-wise PSF-leakage correction: a two-step model of PSF contamination using binned regression in signal-to-noise and galaxy-PSF size ratio (Paper I; Guerrini et al. 2025). We report results from the leakage-corrected catalogs, which are used for cosmological inference in Papers IV and V.

3. Methods

3.1. Two-point correlation measurements

All *B*-mode diagnostics in this analysis use the discrete shear catalog $C = \{(\gamma_i, w_i, \hat{\mathbf{n}}_i)\}_{i=1}^N$, which is composed of complex ellipticities γ_i , metacalibration inverse-variance weights w_i , and sky positions $\hat{\mathbf{n}}_i$ for N source galaxies. The ellipticities γ_i are shear estimates calibrated via metacalibration (Huff & Mandelbaum 2017;

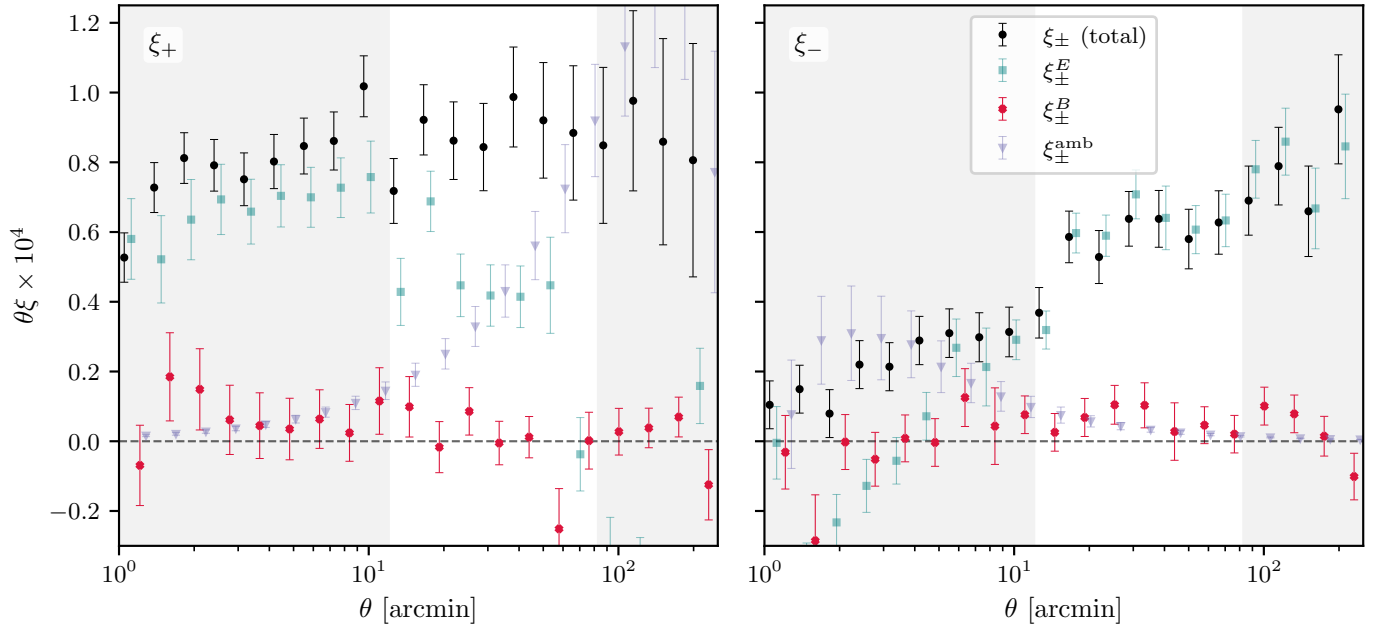


Fig. 1: Pure *E/B*-mode decomposition of the measured shear correlation functions for the fiducial (leakage-corrected) catalog. Panels show ξ_+ (left) and ξ_- (right) decomposed into total (black), *E*-mode (teal), *B*-mode (crimson), and ambiguous (purple) components following Schneider et al. (2022). The *E* modes trace the lensing signal, while *B* modes—which should vanish for pure gravitational lensing—diagnose systematic contamination. Ambiguous modes capture boundary effects from the finite angular range. Shaded regions indicate fiducial scale cuts. Error bars derive from semi-analytical covariance propagation (Section 3.5).

Sheldon & Huff 2017): galaxy images are artificially sheared to measure the shape response R_i , yielding $\gamma_i = (e_i - c_i)/R_i$ from the observed ellipticity e_i and additive bias c_i . The tangential and cross-component correlation functions are defined as the ensemble average of ellipticity products at pair separation θ :

$$\xi_{\pm}(\theta) = \langle \gamma_t(\hat{\mathbf{n}}_i)\gamma_t(\hat{\mathbf{n}}_j) \pm \gamma_x(\hat{\mathbf{n}}_i)\gamma_x(\hat{\mathbf{n}}_j) \rangle_{\theta_{ij}=\theta}, \quad (1)$$

where γ_t and γ_x denote the tangential and cross components of the complex ellipticity in the coordinate frame defined by the pair-separation vector. We weight each pair by the product of metacalibration weights and accumulate contributions in angular bins:

$$\hat{\xi}_{\pm}(\theta_k) = \frac{\sum_{i \neq j} w_i w_j \Pi(\theta_{ij}, \theta_k) [\gamma_{t,i}\gamma_{t,j} \pm \gamma_{x,i}\gamma_{x,j}]}{\sum_{i \neq j} w_i w_j \Pi(\theta_{ij}, \theta_k)}, \quad (2)$$

where $\Pi(\theta_{ij}, \theta_k)$ is the binning kernel selecting pairs with separations in bin k and $\theta_{ij} = \arccos(\hat{\mathbf{n}}_i \cdot \hat{\mathbf{n}}_j)$.

In harmonic space, the analogous statistics are the angular power spectra C_{ℓ}^{EE} and C_{ℓ}^{BB} . From the spin-2 spherical harmonic coefficients $\gamma_{\ell m}^{\alpha}$ (with $\alpha \in \{E, B\}$), the power spectrum is

$$C_{\ell}^{\alpha\beta} = \frac{1}{2\ell + 1} \sum_m \gamma_{\ell m}^{\alpha} \gamma_{\ell m}^{\beta *} \quad (3)$$

These configuration-space (ξ_{\pm}) and harmonic-space (C_{ℓ}) statistics are complementary representations of the same underlying shear field. Both give consistent *B*-mode diagnostics for a clean catalog, but respond differently to systematic contamination: configuration-space pure modes localize contamination at its characteristic angular scale and filter out mask-induced ambiguous modes, while harmonic-space pseudo- C_{ℓ} estimators spread localized features across multipoles through mask-induced mode

coupling and are more sensitive to diffuse shape biases. Cross-validation across both representations exposes systematics that one framework absorbs but the other detects.

We implement the configuration-space estimator using TreeCorr (Jarvis et al. 2004), which evaluates Eq. (2) directly from source positions without intermediate pixelization. We first compute correlation functions on an extended integration grid of 1000 logarithmic bins spanning $\theta = 0.5$ –500 arcmin, then average to a 20-bin logarithmic reporting grid over $\theta = 1$ –250 arcmin matching the range adopted for cosmological inference (Goh et al. 2025). Each reported bin value is a weighted average of the integration-grid measurements, with weights given by the effective pair count $N_{\text{pair}}(\theta)$. Fine binning and extended angular coverage ensure convergence of the pure-mode and COSEBI filter-function integrals: the 1000-bin sampling achieves better than 1 per cent accuracy, and the factor-of-two range extension beyond the reporting boundaries reduces edge effects to negligible levels. We use a single spatial footprint for all measurements (jackknife partitioning is used only for covariance validation tests). Statistical uncertainties are derived from the semi-analytical covariance framework described in Section 3.5.

3.2. Pure *E/B* decomposition

We decompose the measured correlation functions $\xi_{\pm}(\theta)$ into pure *E*-mode, *B*-mode, and ambiguous components following Schneider et al. (2022):

$$\xi_+(\theta) = \xi_+^E(\theta) + \xi_+^B(\theta) + \xi_+^{\text{amb}}(\theta), \quad (4)$$

$$\xi_-(\theta) = \xi_-^E(\theta) - \xi_-^B(\theta) + \xi_-^{\text{amb}}(\theta), \quad (5)$$

Ambiguous modes $\xi_{\pm}^{\text{amb}}(\theta)$ arise from shear patterns that cannot be assigned unique *E*- or *B*-mode origin on a finite angular interval; they take the functional forms $\xi_{\pm}^{\text{amb}}(\theta) = a + b\theta^2$ and

$\xi_-^{\text{amb}}(\theta) = c\theta^{-2} + d\theta^{-4}$. The pure-mode correlation functions are computed from integral transforms over the measured $\xi_{\pm}(\theta)$:

$$\begin{aligned}\xi_+^{\text{E,B}}(\theta) &= \frac{1}{2} \left[\xi_+(\theta) \pm \xi_-(\theta) \pm \int_{\theta}^{\theta_{\max}} \frac{d\theta'}{\theta'} \xi_-(\theta') \left(4 - \frac{12\theta^2}{\theta'^2} \right) \right] \\ &\quad - \frac{1}{2} [S_+(\theta) \pm S_-(\theta)],\end{aligned}\quad (6)$$

$$\begin{aligned}\xi_-^{\text{E,B}}(\theta) &= \frac{1}{2} \left[\xi_+(\theta) \pm \xi_-(\theta) + \int_{\theta_{\min}}^{\theta} \frac{d\theta' \theta'}{\theta^2} \xi_+(\theta') \left(4 - \frac{12\theta^2}{\theta'^2} \right) \right] \\ &\quad - \frac{1}{2} [V_+(\theta) \pm V_-(\theta)],\end{aligned}\quad (7)$$

Here, the + sign gives E -modes and the – sign gives B -modes. The auxiliary functions $S_{\pm}(\theta)$ and $V_{\pm}(\theta)$ enforce boundary conditions that remove ambiguous modes: $\xi_+^{\text{amb}} = S_+$ and $\xi_-^{\text{amb}} = V_-$ (Schneider et al. 2022). $\xi_{\pm}^{\text{B}}(\theta)$ depends only on curl-like shear; any significant detection therefore indicates systematic contamination.

We adopt the publicly available `cosmo_numba` implementation of the Schneider et al. (2022) filter kernels, applying the integral transforms to the binned correlation functions $\hat{\xi}_{\pm}(\theta_k)$ measured on the 1000-bin integration grid. Figure 1 shows the pure E/B decomposition for the fiducial catalog.

3.3. COSEBIs

COSEBIs compress $\xi_{\pm}(\theta)$ into discrete orthogonal modes E_n and B_n with clean E/B separation on finite angular intervals (Schneider et al. 2010). The filter functions $T_{\pm n}(\theta)$ are constructed to satisfy boundary conditions that remove ambiguous modes (Section 3.2). Because the $T_{\pm n}$ are orthonormal, different modes capture largely independent information. Each $T_{\pm n}(\theta)$ oscillates $n+1$ times across the angular interval; higher-order modes are therefore sensitive to systematic signatures at correspondingly finer angular scales.

We compute COSEBIs over a given angular range $[\theta_{\min}, \theta_{\max}]$ arcmin using logarithmic filter functions:

$$E_n = \frac{1}{2} \int_{\theta_{\min}}^{\theta_{\max}} d\theta \theta [T_{+n}(\theta) \xi_+(\theta) + T_{-n}(\theta) \xi_-(\theta)], \quad (8)$$

$$B_n = \frac{1}{2} \int_{\theta_{\min}}^{\theta_{\max}} d\theta \theta [T_{+n}(\theta) \xi_+(\theta) - T_{-n}(\theta) \xi_-(\theta)]. \quad (9)$$

Figure 2 shows COSEBI B -mode amplitudes for the first $n_{\max} = 20$ modes for the fiducial catalog. For logarithmic COSEBIs, E -mode cosmological information saturates by $n \approx 5-6$ for typical parameter constraints (Ω_m, σ_8). We therefore report B -mode probability-to-exceed (PTE) statistics for both $n \leq 6$ and $n \leq 20$; the twenty-mode statistic is more sensitive to systematic contamination. Higher-order COSEBI modes ($n > 6$) have increasingly oscillatory sensitivity to additive systematics; these patterns can identify systematic type, as prior Stage-III analyses show (Asgari et al. 2019).

The COSEBI coefficients can reconstruct pure-mode correlation functions (Section 3.2):

$$\xi_{\pm}^{\text{E}}(\theta) = \frac{\bar{\theta}^2}{\beta_{\theta}} \sum_{n=1}^{n_{\max}} E_n T_{\pm n}(\theta), \quad (10)$$

$$\xi_{\pm}^{\text{B}}(\theta) = \frac{\bar{\theta}^2}{\beta_{\theta}} \sum_{n=1}^{n_{\max}} B_n T_{\pm n}(\theta), \quad (11)$$

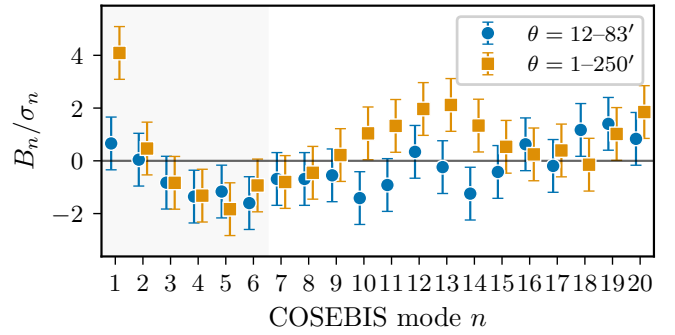


Fig. 2: COSEBI B -mode amplitudes for the fiducial catalog, normalized by uncertainty (B_n/σ_n). Blue circles: fiducial scale-cut range 12–83 arcmin; orange squares: full measurement range 1–250 arcmin. The shaded region highlights mode numbers $n \leq 6$, which capture nearly all cosmological information. On the full range, mode $n = 1$ shows a $> 4\sigma$ excess with oscillatory structure through $n \approx 5$ —a pattern consistent with repeating additive shear bias seen in CFHTLenS and KiDS-450 (Asgari et al. 2019). Scale cuts suppress the first-mode excess to below 1σ and largely eliminate the oscillatory signature.

Here $\bar{\theta} = (\theta_{\min} + \theta_{\max})/2$ and $\beta_{\theta} = (\theta_{\max} - \theta_{\min})/(\theta_{\max} + \theta_{\min})$. We use direct integral transforms for the pure-mode measurements. COSEBIs require consistent angular ranges for ξ_+ and ξ_- , while the pure-mode integral transforms (Eqs. 6–7) permit independent scale cuts for each.

3.4. Catalog-based harmonic-space power spectra

We estimate C_{ℓ}^{EE} and C_{ℓ}^{BB} (Eq. 3) directly from the discrete catalog as an independent cross-check on the real-space B -mode diagnostics. We use the catalog-based pseudo- C_{ℓ} approach of Wolz et al. (2025), which evaluates spin-2 spherical harmonic transforms directly at source positions without intermediate pixelization. The mask is represented as a set of delta functions at source positions, and the spherical harmonic transforms are evaluated on this irregular grid using the `ducc` library (Reinecke & Seljebotn 2023). The mode-coupling matrix corrects for mask geometry as in standard pseudo- C_{ℓ} estimation, but with an analytic shot-noise subtraction that stabilizes the estimator at low source densities. The raw pseudo- C_{ℓ} requires debiasing for measurement noise and mask shot noise; see Wolz et al. (2025) for the estimator and Paper V for the full UNIONS implementation. We bin into 32 bandpowers with square-root spacing ($\ell^{0.5}$) over $50 \leq \ell \leq 2000$, with fiducial scale cuts at $300 < \ell < 1600$. Figure 3 shows the measured C_{ℓ}^{BB} and C_{ℓ}^{EB} for the fiducial catalog.

3.5. Covariance estimation

Jackknife methods suffer from limited effective sample size given the survey geometry and spatial correlations, producing noisy covariance estimates. We therefore adopt a semi-analytical approach for the pure-mode correlation covariances, combining theoretical covariances from `CosmoCov` (Krause & Eifler 2017; Fang et al. 2020) with Monte Carlo propagation through the pure-mode transforms.

First, we compute theoretical Gaussian covariance matrices for $\xi_{\pm}(\theta)$ on the 1000-bin logarithmic integration grid spanning $\theta = 0.5$ –500 arcmin, using survey properties from Table 2 in Pa-

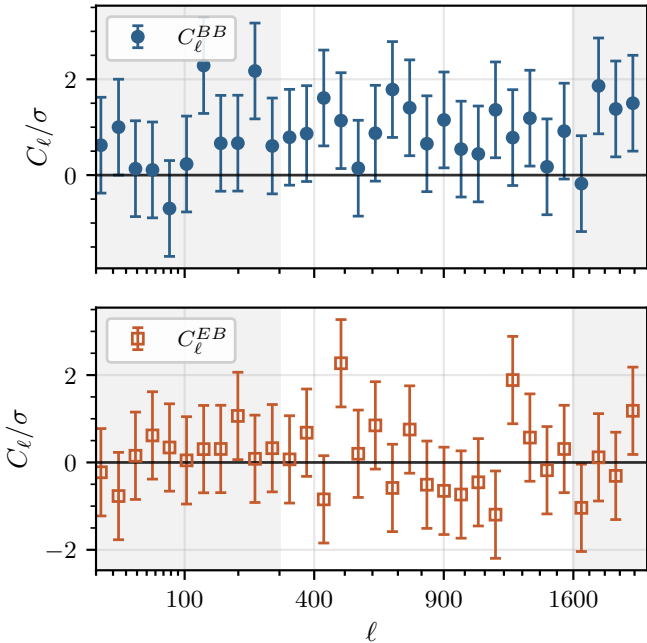


Fig. 3: Harmonic-space power spectra for the fiducial catalog (leakage-corrected), normalized by uncertainty. Top: *B*-mode auto-power C_ℓ^{BB}/σ ; bottom: *E*-*B* cross-power C_ℓ^{EB}/σ . C_ℓ^{BB} scatters predominantly positive but yields an acceptable PTE. C_ℓ^{EB} scatters symmetrically around zero, indicating that any *B*-mode contamination is uncorrelated with the lensing signal.

per I and the Planck 2018 fiducial cosmology (Planck Collaboration 2020). The 1000-bin grid matches the TreeCorr measurement binning exactly. CosmoCov computes the Gaussian (disconnected) contribution through numerical integration over the survey geometry, accounting for the footprint’s impact on mode coupling but neglecting connected trispectrum terms and super-sample covariance.

Second, we propagate the ξ_{\pm} Gaussian covariance through the pure-mode filter functions via Monte Carlo sampling. We draw $N_{\text{samples}} = 2000$ realizations of $\xi_{\pm}(\theta)$ from the CosmoCov covariance matrix on the integration grid, apply the integral transforms in Eqs. (6)–(7) to each realization, and compute empirical covariances of the reconstructed pure-mode functions $\xi_{\pm}^{\text{E/B}}(\theta)$. This captures the full correlation structure: cross-covariance between ξ_+ and ξ_- , correlations between *E/B*/ambiguous mode types, and angular-bin correlations from the overlapping filter-function support. The 2000-sample ensemble achieves per cent level convergence in the derived covariance elements. When computing χ^2 statistics for PTE assessments, we apply the Hartlap correction factor $(N_{\text{samples}} - N_{\text{obs}} - 2)/(N_{\text{samples}} - 1)$ (Hartlap et al. 2007) to the inverse covariance to account for the positive bias from finite sample sizes.

COSEBI covariances are computed directly from the theoretical ξ_{\pm} covariance via $\mathbf{C}_{B_n B_m} = \mathbf{T}^T \mathbf{C}_\xi \mathbf{T}$, where \mathbf{T} encodes the filter functions. The C_ℓ^{BB} covariance uses Gaussian contributions from NaMaster’s mode-coupling framework. The NaMaster *BB* pixel-space covariance exhibits sample-variance-like power at low ℓ , where the mode-coupling matrix can be unstable (Alonso et al. 2019, Section 4.3). Paper V tests the *B*-mode covariance against 10 000 Gaussian simulations and finds agreement at the 5 per cent level for $\ell > 100$ (Appendix C therein).

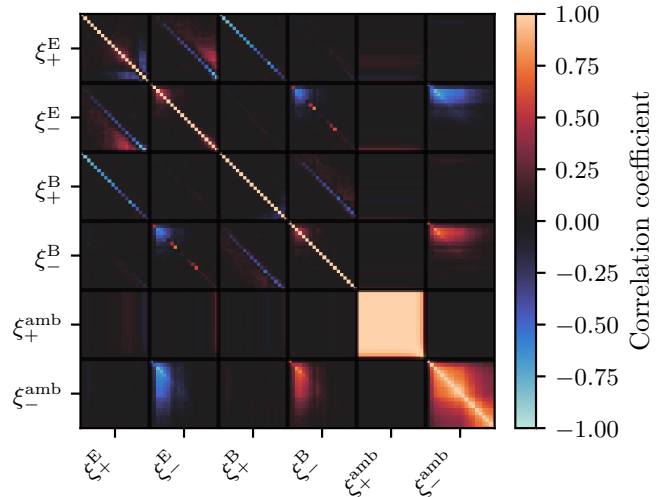


Fig. 4: Pure *E*/*B*-mode correlation-function covariance matrix for the fiducial catalog (leakage-corrected) from semi-analytical propagation of 2000 Monte Carlo realizations. The matrix is organized into six blocks: ξ_+^E , ξ_-^E , ξ_+^B , ξ_-^B , ξ_+^{amb} , ξ_-^{amb} , with 20 angular bins per block. Off-diagonal correlations arise from integral coupling in the pure-mode filters.

Our adopted $\ell_{\min} = 300$ cut, motivated primarily by *B*-mode outliers at $\ell \approx 125$ and 250 (Section 4), also excludes the covariance-unstable regime. Non-Gaussian terms are omitted for the *B*-mode null tests; since Gaussian-only covariance underestimates the true uncertainties, passing a null test with underestimated errors is conservative. For C_ℓ^{EE} cosmological inference, Paper V uses a combined Gaussian (iNKA) plus non-Gaussian (OneCovariance) covariance. Figure 4 shows the pure *E*/*B* covariance structure.

The primary limitation is the Gaussian-only approximation. Non-Gaussian contributions—connected trispectrum and super-sample covariance (variance from density modes larger than the survey footprint)—inflate UNIONS variances by 1.1–1.3× across the angular scales used here. Full non-Gaussian covariance computation on the 1000-bin integration grid is computationally prohibitive. Omitting these terms underestimates uncertainties; the reported PTEs are biased low, making our passing null tests conservative.

3.6. *B*-mode significance

We assess *B*-mode significance across a grid of angular scale cut combinations. For each scale range, we compute a χ^2 statistic testing the *B*-mode data vector \mathbf{d}_B against zero:

$$\chi_B^2 = \mathbf{d}_B^T \mathbf{C}_{BB}^{-1} \mathbf{d}_B, \quad (12)$$

where \mathbf{C}_{BB} is the *B*-mode covariance submatrix for the selected scale range (Hartlap-corrected for the MC-propagated pure-mode covariance; Section 3.5). The probability-to-exceed (PTE) is then $P(\chi^2 > \chi_B^2 | v)$ for v degrees of freedom equal to the number of data points in the range. For the pure-mode decomposition, we compute PTEs separately for ξ_+^B and ξ_-^B , as well as a joint test ξ_{tot}^B using the concatenated data vector and full cross-covariance. For COSEBIs, we evaluate PTEs using both $n \leq 6$ and $n \leq 20$ (Section 3.3). For C_ℓ^{BB} , we apply the same framework across multipole ranges.

Table 1: B -mode PTE values for the fiducial catalog (leakage-corrected) at fiducial and full-range scale cuts. Bold values indicate $\text{PTE} < 0.05$ (null-test failure).

Scale cuts	COSEBIS		Pure E/B			Pseudo- C_ℓ
	$B_n (n \leq 6)$	$B_n (n \leq 20)$	ξ_+^B	ξ_-^B	ξ_{tot}^B	C_ℓ^{BB}
Fiducial	0.78	0.94	0.30	0.27	0.20	0.39
Full range	1.37×10^{-5}	1.08×10^{-4}	0.42	0.17	0.42	0.13

3.7. Mock validation

We validate the full analysis pipeline on 350 GLASS lognormal mocks (Tessore et al. 2023) that share the survey’s galaxy positions, weights, and Planck 2018 cosmology. The pure E/B decomposition and COSEBIs produce B -modes consistent with zero across all mock realizations, confirming that both decompositions are unbiased for noise-dominated data. For the harmonic-space power spectra, the distribution of per-multipole-range PTEs is uniform (Kolmogorov-Smirnov $p = 0.31$, $\langle \text{PTE} \rangle = 0.50$), confirming that our B -mode significance estimates are well calibrated.

4. Results

The three B -mode statistics collectively detect contamination at both large and small angular scales, but the fiducial catalog passes all null tests after scale cuts (Table 1). The adopted scale cuts, informed by additional systematics tests and blinded inference checks (Paper IV), are more conservative than B -mode PTEs alone would require.

4.1. Fiducial catalog

The pure E/B decomposition (Figure 1) reveals two features in ξ_+^B : a 4σ single-bin outlier at $\theta \approx 3$ arcmin (not replicated across catalog versions; Section 5) and a 2σ excess at $\theta \approx 10$ arcmin that persists across all versions (Section 5). ξ_+^B shows correlated deviations at large scales that drive PTE failures when $\theta_{\text{max}} \gtrsim 83$ arcmin (Figure 6). On the fiducial scale-cut range 12–83 arcmin, both pass null tests (PTE = 0.30 for ξ_+^B , 0.27 for ξ_-^B , 0.20 for the joint test); on the full range, ξ_+^B fails (PTE = 0.42) while ξ_-^B passes (PTE = 0.17).

COSEBI B -mode amplitudes (Figure 2) show a $> 4\sigma$ first-mode excess on the full angular range 1–250 arcmin, driving an oscillatory pattern through higher modes characteristic of the repeating additive bias seen in CFHTLenS and KiDS-450 (Asgari et al. 2019) (full-range PTE = 1.37×10^{-5} for $n \leq 6$). Scale cuts suppress the first-mode excess to below 1σ and the PTE improves to 0.78.

In harmonic space (Figure 3), C_ℓ^{BB} shows outliers at $\ell \approx 125$ and 250 and at $\ell \gtrsim 1600$; the fiducial range $300 < \ell < 1600$ yields PTE = 0.39. The full multipole range also passes (PTE = 0.13). C_ℓ^{EB} is consistent with zero, indicating the B -mode contamination is uncorrelated with the lensing signal.

Figures 5 and 6 map PTE across scale cuts for all three statistics, revealing broad regions of acceptance around the adopted cuts (12–83 arcmin in configuration space, $300 < \ell < 1600$ in harmonic space). The adopted cuts are not fine-tuned: moving them by several bins in either direction does not change the null-test outcome.

4.2. Catalog comparison

Figures 7 and 8 compare B -mode measurements across catalog versions. The key pattern is selective failure: different statistics fail for different catalog variants, and only the fiducial passes all tests (Table B.1).

In configuration space, the fiducial catalog passes both pure-mode null tests (ξ_+^B PTE = 0.30, ξ_-^B PTE = 0.27). The initial catalog passes ξ_+^B (PTE = 0.51) but fails ξ_-^B (PTE = **0.005**) and the joint test (PTE = **0.030**). The masked catalog fails ξ_+^B (PTE = **0.020**) and the joint test (PTE = **0.014**), while ξ_-^B passes (PTE = **0.047**). The relaxed-flags catalog passes both individual statistics (ξ_+^B PTE = 0.78, ξ_-^B PTE = **9.40×10^{-4}**) but fails the joint test (PTE = **0.014**). COSEBI $B_n (n \leq 6)$ tests pass for all four versions (PTE = 0.94, 0.78, 0.60, 0.82), despite pure-mode and harmonic-space failures (Table B.1). Figure 9 shows COSEBI B_n/σ_n for all four versions at both the full angular range and the fiducial scale cuts. At full range, the oscillatory pattern driven by the 10 arcmin feature is visible across low-order modes for all versions; at fiducial cuts, all versions scatter within $\pm 2\sigma$ across all twenty modes.

An approximately 10 arcmin feature in ξ_+^B , consistent with a camera-scale systematic, reaches $\approx 2\sigma$ in the initial and fiducial catalogs and 3.4σ in the masked catalog, where the halo masks make it more prominent.

In harmonic space at the fiducial multipole range, the initial and relaxed-flags catalogs fail (C_ℓ^{BB} PTE = **0.004**, **1.12×10^{-9}**), while the fiducial and masked catalogs pass (PTE = 0.39, 0.45).

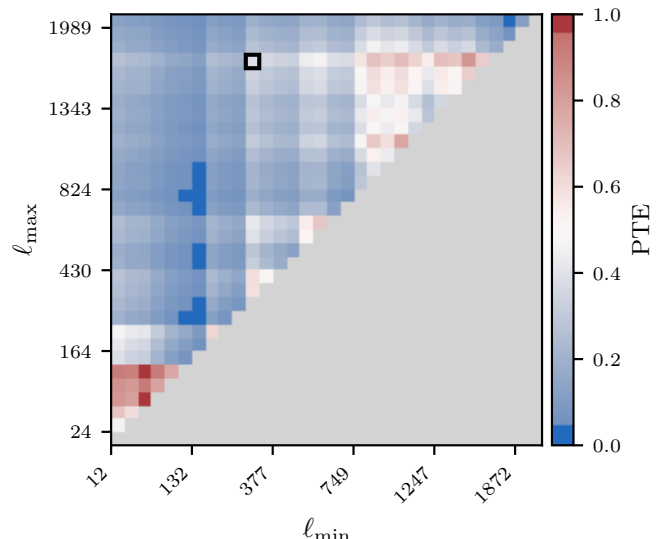


Fig. 5: Harmonic-space C_ℓ^{BB} PTE as a function of multipole range $[\ell_{\text{min}}, \ell_{\text{max}}]$ for the fiducial catalog. Blues indicate significant B modes (failing PTEs); whites and reds indicate consistency with zero. Failures cluster where $\ell_{\text{min}} \lesssim 200$ and the range includes outliers near $\ell \approx 125$ or 250 (cf. Figure 3).

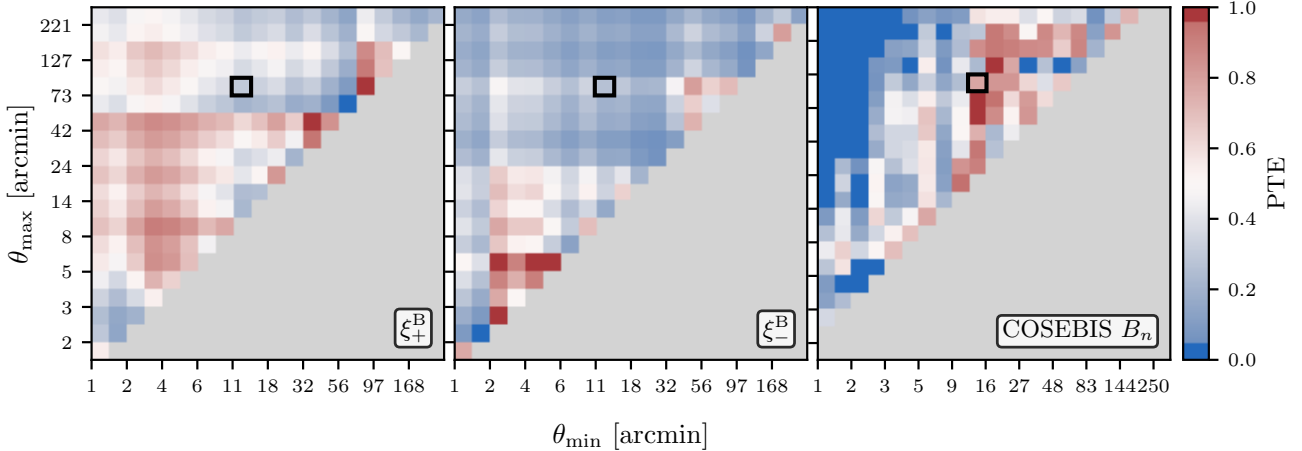


Fig. 6: Two-dimensional probability-to-exceed (PTE) maps for the fiducial catalog (leakage-corrected). Panels show ξ_+^B (left), ξ_-^B (center), and COSEBI B_n (right) PTEs as a function of lower (θ_{\min} , horizontal) and upper (θ_{\max} , vertical) angular scale cuts. Blues indicate significant B modes ($\text{PTE} < 0.05$); whites and reds indicate consistency with zero. Black squares mark the adopted scale cuts (12–83 arcmin). ξ_+^B shows significant B modes on scales $\lesssim 4$ arcmin; ξ_-^B produces low PTEs over a wide range of upper scale cuts, but only causes failures for $\theta_{\max} \gtrsim 83$ arcmin. PTE maps for the initial and masked catalog variants appear in Appendix B.

Both the initial and relaxed-flags catalogs fail null tests in both representations.

COSEBI PTEs ($n \leq 6$) pass at fiducial scale cuts with or without the leakage correction, indicating that the scale cuts already exclude the ranges most affected by PSF leakage. Paper V reports that the object-wise correction reduces residual galaxy–PSF correlations to below 5 per cent of the signal on most multipoles.

5. Discussion

The most informative feature of this analysis is not that scale cuts yield clean null tests—that was the design—but the pattern of failures across catalog versions and statistical frameworks. Configuration-space and harmonic-space estimators fail on different catalog variants (Table B.1), revealing complementary systematic sensitivities that no single statistic captures alone.

Size cuts (initial → fiducial) cure both the ξ_+^B failure (PTE from **0.005** to 0.27) and the harmonic-space failure (PTE from **0.004** to 0.39), with ξ_+^B acceptable in both (PTE = 0.51, 0.30). Poorly resolved galaxies appear to introduce PSF-related shape bias, producing excess signal in both ξ_-^B and harmonic-space estimators—each more sensitive to high-multipole contamination—while ξ_+^B is less affected. Star masking (masked catalog) shows the opposite pattern: ξ_+^B fails (PTE = **0.020**) while ξ_-^B passes (PTE = **0.047**) and harmonic space passes (PTE = 0.45). The halo masks excise circular regions around bright stars, imprinting angular structure in the effective survey window at the stellar-halo scale; this mask geometry amplifies the ξ_+^B excess near 10 arcmin (Section 4). The relaxed-flags catalog fails in harmonic space (PTE = **1.12 × 10⁻⁹**, more severely than the initial catalog) and in the joint configuration-space test (PTE = **0.014**), though both individual statistics pass; deblended objects appear to introduce systematic contamination visible across both spaces. Only the fiducial catalog passes all tests in both representations; Papers IV and V use the same fiducial.

All four catalog versions pass COSEBI null tests ($n \leq 6$) at fiducial cuts. At fiducial scale cuts, the dominant 10 arcmin feature is already excised, and version-to-version residual differ-

ences are consistent with noise in the low-order modes carrying cosmological information. The universal pass does not imply an intrinsically clean COSEBI spectrum: on the full angular range, the 10 arcmin feature contaminates multiple low-order modes, but scale cuts excise those scales before COSEBI integration. For the fiducial catalog, both the first six modes (PTE = 0.78) and the full twenty (PTE = 0.94) pass; other versions show similar results (Table B.1).

ξ_-^B is the most failure-prone configuration-space statistic: ξ_-^B receives contributions from higher multipoles than ξ_+^B at fixed angular separation and is consequently more sensitive to PSF-leakage systematics (Crittenden et al. 2002). The object-wise leakage correction reduces galaxy–PSF correlations in both E and B modes (Paper V) but does not eliminate ξ_-^B sensitivity: higher-order PSF moments, in particular fourth-order terms, contribute B -mode power that a second-order model cannot capture (Zhang et al. 2023). The correction’s uneven impact across statistics and versions is consistent with PSF leakage being one contributor among several.

The 10 arcmin ξ_+^B excess (Section 4) is the most significant unresolved systematic in this analysis. It does not arise from high-leakage galaxies—size cuts leave it unchanged—and is not an artifact of mask geometry, though masking amplifies the feature from 2σ to 3.4σ without shifting its angular scale. Paper V identifies a corresponding peak in the harmonic-space galaxy–PSF power spectrum $C_\ell^{\tau_0}$ at $\ell \approx 1000$ —the Hankel-transform counterpart of $\theta \approx 10$ arcmin. Paper I finds no matching peak in the configuration-space τ_0 correlation function, suggesting a higher-order PSF-leakage or selection-function effect localized to camera geometry.

The full-range COSEBI oscillations (Section 4) place the 10 arcmin feature in a known systematic class. Asgari et al. (2019) showed that detector-level effects fixed in focal-plane coordinates—per-CCD electronic bias—stamp the same additive shear pattern onto each survey pointing, creating structure in the B -mode shear field at the characteristic angular scale of the camera geometry. MegaCam’s 40 CCDs (Boulade et al. 2003) span 6–14 arcmin individually; the 10 arcmin ξ_+^B excess sits squarely within this range. Because COSEBIs decompose B

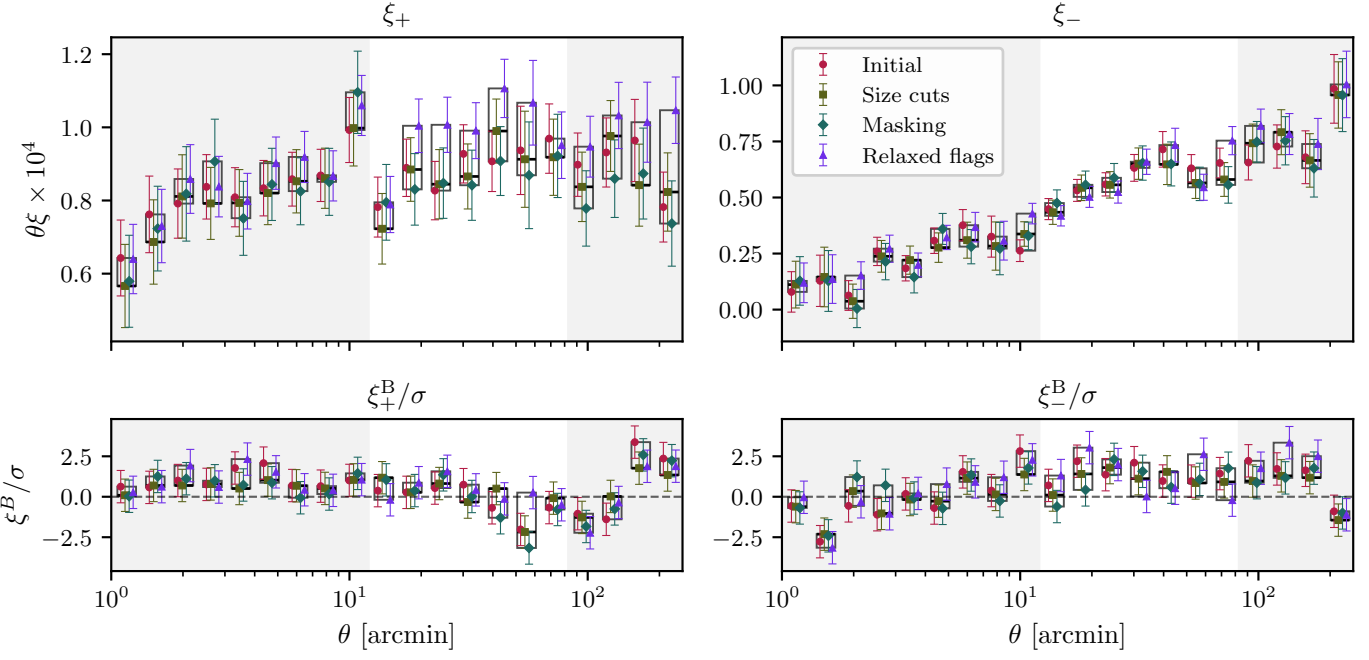


Fig. 7: Pure E/B -mode correlation functions across catalog versions: initial (blue), fiducial (orange), masked (teal), and relaxed-flags (purple). Top row: correlation functions ξ_+ (left) and ξ_- (right) scaled by θ . Bottom row: B -mode components ξ_+^B/σ and ξ_-^B/σ normalized by uncertainty. In each bin, the rectangle spans the range of values across all versions and the horizontal line marks the fiducial value. Shaded bands mark the fiducial scale cuts. The masked catalog shows an approximately 3σ excess at $\theta \approx 10$ arcmin in ξ_+ , an amplified camera-scale systematic that drives its configuration-space null-test failure. The fiducial, initial, and relaxed-flags catalogs are consistent within uncertainties across the fiducial range.

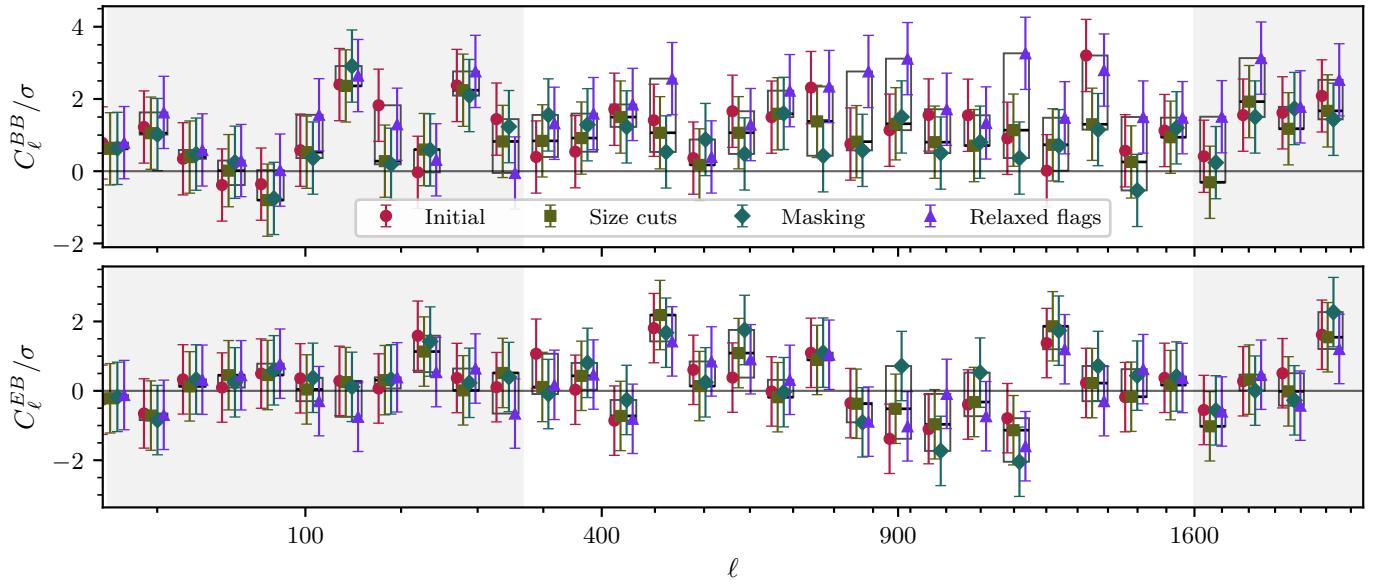


Fig. 8: Same as Figure 7, but for harmonic-space power spectra. Top: C_ℓ^{BB}/σ ; bottom: C_ℓ^{EB}/σ . The initial and relaxed-flags catalogs show elevated scatter, driving their harmonic-space null-test failures. The fiducial and masked catalogs are consistent with zero across the full range.

modes into orthogonal modes over a finite angular range, a feature localized in angle requires many modes to represent it, producing an oscillatory high- n signature. Asgari et al. (2019) identified this pattern in CFHTLenS—which used the same Mega-Cam camera—and in KiDS-450. We observe the same signature through $n \approx 5$. Scale cuts that exclude the 10 arcmin feature

simultaneously suppress the oscillatory COSEBI pattern, reducing the first-mode deviation from $> 4\sigma$ to below 1σ and yielding acceptable PTEs. The adopted lower cut of 12 arcmin lies 1.4 arcmin above the feature’s peak at $\theta \approx 10.6$ arcmin; this offset is sufficient because the feature is narrowly localized in angle. The 4σ single-bin outlier at $\theta \approx 3$ arcmin in the fiducial catalog

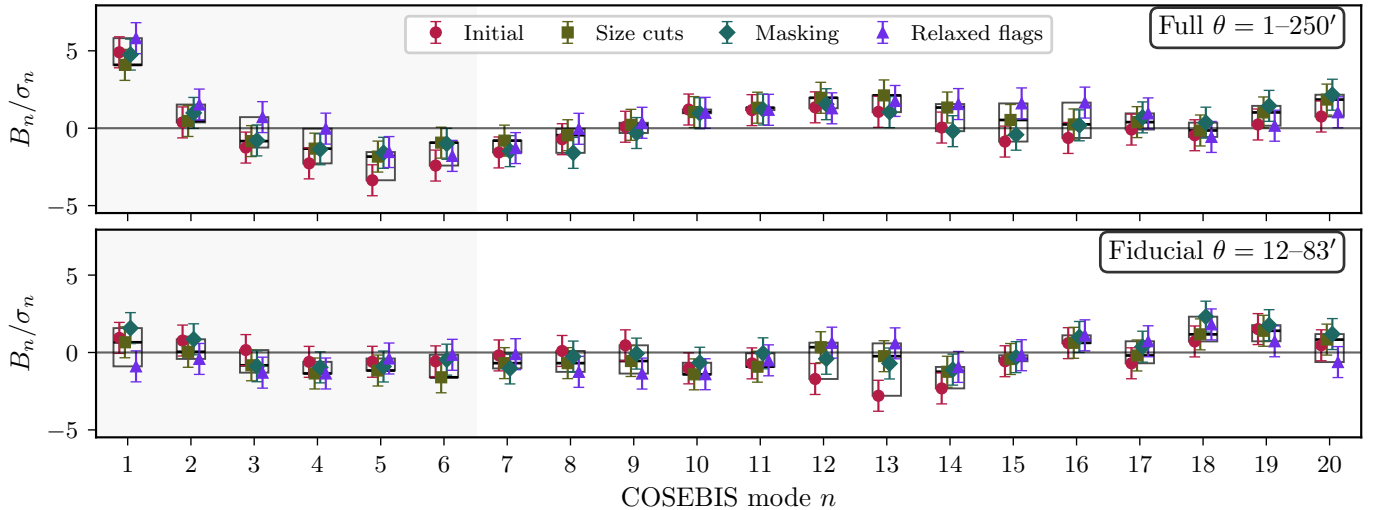


Fig. 9: Same as Figure 7, but for COSEBI B -mode amplitudes B_n/σ_n at two angular ranges. Top: full range $\theta = 1\text{--}250'$ arcmin, where the 10 arcmin systematic produces coherent deviations across low-order modes. Bottom: fiducial scale cuts $\theta = 12\text{--}83'$ arcmin, where all versions pass the B -mode null test ($n \leq 6$). At fiducial cuts, the contamination is excised and all four catalogs yield B -modes consistent with zero.

(Section 4) does not appear in any other version at comparable significance, consistent with a noise fluctuation; the fiducial lower scale cut excludes it.

Configuration-space and harmonic-space estimators respond differently to the same contamination. First, pure-mode and COSEBI statistics resolve contamination at its characteristic angular scale, so a narrow cut around $\theta \approx 10$ arcmin suffices to excise it. Harmonic-space pseudo- C_ℓ estimators spread localized angular-space features across broad ℓ -ranges through mask-induced mode coupling (Alonso et al. 2019); NaMaster corrects for this in the ensemble average but not in individual realizations, so broader multipole cuts are needed. Second, pure-mode and COSEBI filters discard ambiguous modes (Section 3.2) that cannot be uniquely classified as E or B , whereas harmonic-space estimators assign all power to C_ℓ^{EE} or C_ℓ^{BB} , absorbing mask-induced E -to- B leakage that the real-space filters exclude by construction. We verify this directly in Appendix A by computing COSEBIs from the harmonic-space bandpowers. The low-order B -modes agree between the two paths: at fiducial scale cuts, both pass; at the full range, both fail, consistent with the 10 arcmin excess driving a significant B_1 . In all three frameworks, Gaussian-only covariance underestimates variances for UNIONS’ geometry, so reported PTEs are conservative throughout.

6. Conclusions

We validate UNIONS B modes using pure-mode correlation functions, COSEBIs, and harmonic-space power spectra. The fiducial catalog passes all three null tests: pure-mode PTEs of 0.30 (ξ_+^B) and 0.27 (ξ_-^B), COSEBI PTE = 0.78, pseudo- C_ℓ PTE = 0.39. Of four catalog variants tested, only the fiducial passes across all statistics; the other three fail selectively—configuration-space or harmonic-space or both—exposing systematics that no single estimator captures alone (Table B.1). All three statistics independently favor consistent scale cuts: ξ_+ and ξ_- on 12–83 arcmin in configuration space, $300 < \ell < 1600$ in harmonic space.

A persistent approximately 10 arcmin ξ_+^B excess—at the angular scale of individual MegaCam CCDs and consistent with repeating additive shear bias (Asgari et al. 2019)—remains unresolved, motivating conservative cuts. At fiducial scale cuts, all four catalog versions pass COSEBI null tests ($n \leq 6$): the residual systematics do not compromise the modes carrying cosmological information.

Differences in tomographic binning, angular-scale choices, and null-test thresholds complicate direct comparison. KiDS-Legacy (Wright et al. 2025) reports tomographic COSEBI p -values of 0.04 (six modes) and 0.09 (twenty modes) after astrometric masking, against a $p = 0.01$ threshold. DES Y3 yields PTE = 0.16 for the non-tomographic B -mode power spectrum (Abbott et al. 2022). HSC Y3 detects significant B modes requiring scale cuts at $\ell = 300$ (Li et al. 2023). UNIONS reports a non-tomographic COSEBI PTE of 0.78 ($n \leq 6$), well above the adopted 0.05 threshold. The validated scale cuts underpin the non-tomographic cosmic shear cosmology in Papers IV and V. These methods—blinded scale selection via B -mode PTE heatmaps, multi-statistic cross-validation, catalog refinement driven by null-test diagnostics—apply directly to Stage-IV surveys, where no single estimator suffices.

Acknowledgements. TBD

Appendix A: Harmonic–configuration space cross-validation via COSEBIs

The COSEBI E_n and B_n modes, defined in Eqs. (8)–(9) as integrals over $\xi_{\pm}(\theta)$, can equivalently be computed from harmonic-space power spectra. The harmonic-space COSEBI modes are

$$E_n = \sum_i \frac{\Delta\ell_i \ell_i}{2\pi} W_n(\ell_i) C_{\ell_i}^{EE}, \quad (\text{A.1})$$

$$B_n = \sum_i \frac{\Delta\ell_i \ell_i}{2\pi} W_n(\ell_i) C_{\ell_i}^{BB}, \quad (\text{A.2})$$

where $W_n(\ell)$ are the harmonic-space COSEBI filter functions (Fourier duals of $T_{\pm n}(\theta)$, computed via FFT-log) and the sum runs over 96 square-root-spaced bandpower bins. Each $W_n(\ell)$ oscillates $n+1$ times, mirroring its real-space counterpart; the 96-bin bandpowers resolve these oscillations adequately for modes $n \leq 8$ but not for higher modes, where the $W_n(\ell)$ amplitudes fall to $\sim 10^{-14}$ and numerical precision limits the transform accuracy.

We compare the two methods over two angular ranges: the full range (1–250 arcmin) and the fiducial scale cuts (12–83 arcmin). Figure A.1 shows the full-range comparison for the fiducial catalog. E -modes agree for the first eight modes; higher modes diverge as numerical precision limits the transform (gray region). B -modes are consistent between the two methods across all twenty modes—including the high- n regime where E -modes diverge. The E -mode signal is spectrally structured, so faithfully reconstructing E_n at high n requires resolving the rapid oscillations of $W_n(\ell)$ against a varying spectrum. The B -mode signal is noise-dominated and approximately flat in ℓ , so fine ℓ -resolution is unnecessary and both paths agree.

At fiducial scale cuts (Figure A.1, lower panel), both methods produce B -modes consistent with zero: the harmonic-space PTE is 0.84 and the configuration-space PTE is 0.60 (modes $n \leq 8$, fiducial catalog). By contrast, both full-range comparisons fail because the 10 arcmin systematic (Section 5) drives a significant B_1 .

Appendix B: PTE heatmaps for additional catalog versions

Figures B.1 and B.2 show harmonic-space and configuration-space PTE heatmaps for all four catalog versions. In harmonic space, the fiducial and masked catalogs show broad acceptance regions, while the initial and relaxed-flags catalogs fail across most multipole combinations. In configuration space, the size cut (fiducial versus initial) expands the acceptance region, while stellar masking contracts it. The relaxed-flags catalog has a similar acceptance region to the fiducial in ξ_{+}^B , but a narrower one in ξ_{-}^B , with the failure boundary encroaching on the fiducial scale cut (PTE = 9.40×10^{-4} at the fiducial scale cut).

Table B.1 compares B -mode PTEs across all four catalog versions at both fiducial and full-range scale cuts. At fiducial cuts, the masked catalog fails ξ_{+}^B due to mask-induced B -mode structure; the initial catalog fails both ξ_{-}^B and harmonic space; and the relaxed-flags catalog fails the joint configuration-space test and harmonic space. Only the fiducial catalog passes all statistics. Full-range PTEs are substantially worse for all versions, particularly COSEBIs ($n \leq 6$), where the oscillatory pattern drives PTEs to 10^{-5} or below.

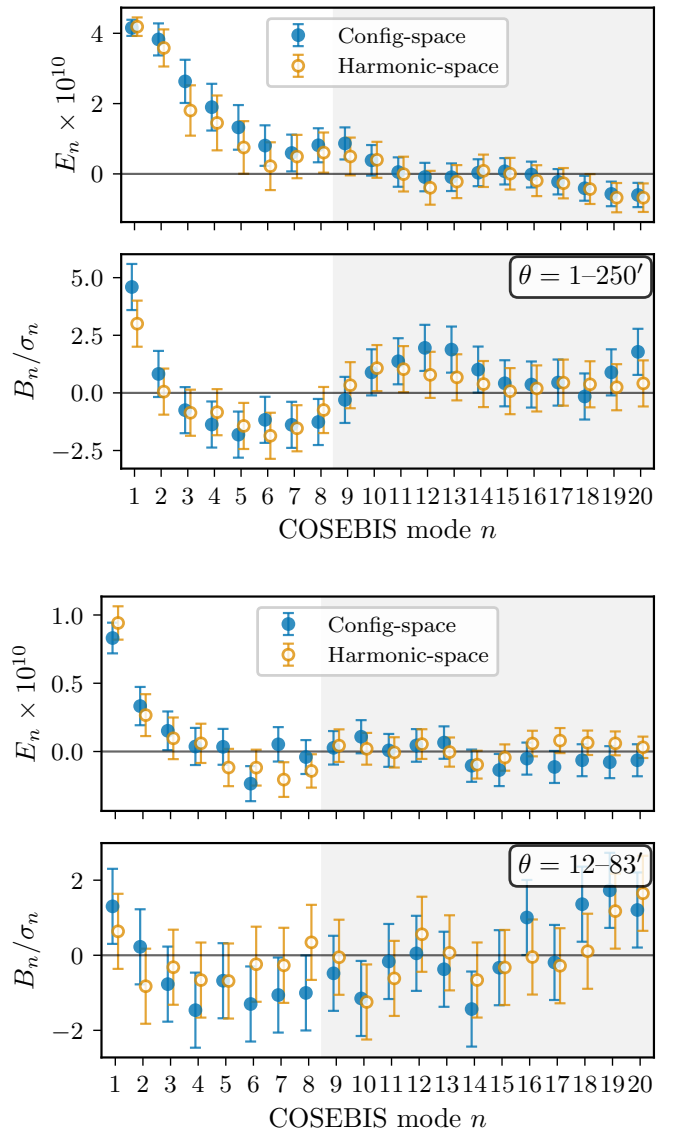
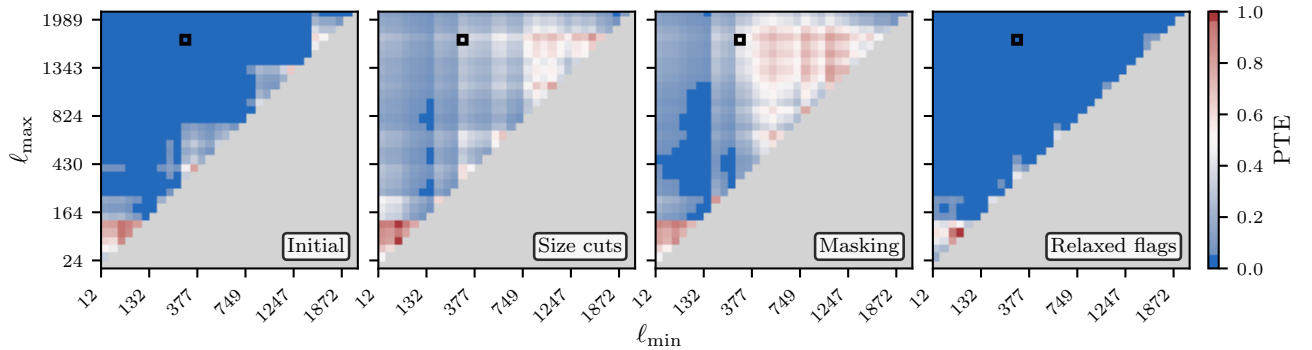


Fig. A.1: COSEBI E_n (top sub-panels) and B_n/σ_n (bottom sub-panels) for the fiducial catalog, computed from configuration-space ξ_{\pm} (filled circles) and harmonic-space pseudo- C_{ℓ} (open circles). *Top:* full angular range 1–250 arcmin. *Bottom:* fiducial scale cuts (12–83 arcmin). Gray shading marks modes $n > 8$, where numerical precision of the $W_n(\ell)$ filter functions limits the transform.

Table B.1: B -mode PTE values across catalog versions at fiducial and full-range scale cuts. Bold values indicate $\text{PTE} < 0.05$ (null-test failure).

Version	Scale cuts	COSEBIS		Pure E/B		Pseudo- C_ℓ
		$B_n (n \leq 6)$	$B_n (n \leq 20)$	ξ_+^B	ξ_-^B	ξ_{tot}^B
Initial (v1.4.5)	Fiducial	0.94	0.61	0.51	0.005	0.030
	Full range	7.37×10^{-10}	4.15×10^{-7}	0.026	7.71×10^{-4}	0.004
Size cuts (fiducial)	Fiducial	0.78	0.94	0.30	0.27	0.20
	Full range	1.37×10^{-5}	1.08×10^{-4}	0.42	0.17	0.42
Masked (v1.4.8)	Fiducial	0.60	0.81	0.020	0.047	0.014
	Full range	4.94×10^{-6}	2.50×10^{-5}	0.039	0.020	0.018
Relaxed flags (v1.4.11.3)	Fiducial	0.82	0.83	0.78	9.40×10^{-4}	0.014
	Full range	1.70×10^{-10}	1.16×10^{-8}	0.10	2.94×10^{-6}	9.07×10^{-4}
						1.12×10^{-9}
						1.78×10^{-12}

**Fig. B.1:** Harmonic-space C_ℓ^{BB} PTE maps for all four catalog versions (Paper I, Table 2). Blues indicate failing PTEs; whites and reds indicate consistency with zero. The initial and relaxed-flags catalogs show widespread failures across multipole ranges. The fiducial catalog has isolated failure regions near $\ell \approx 125-250$. The masked catalog passes across nearly all multipole combinations.

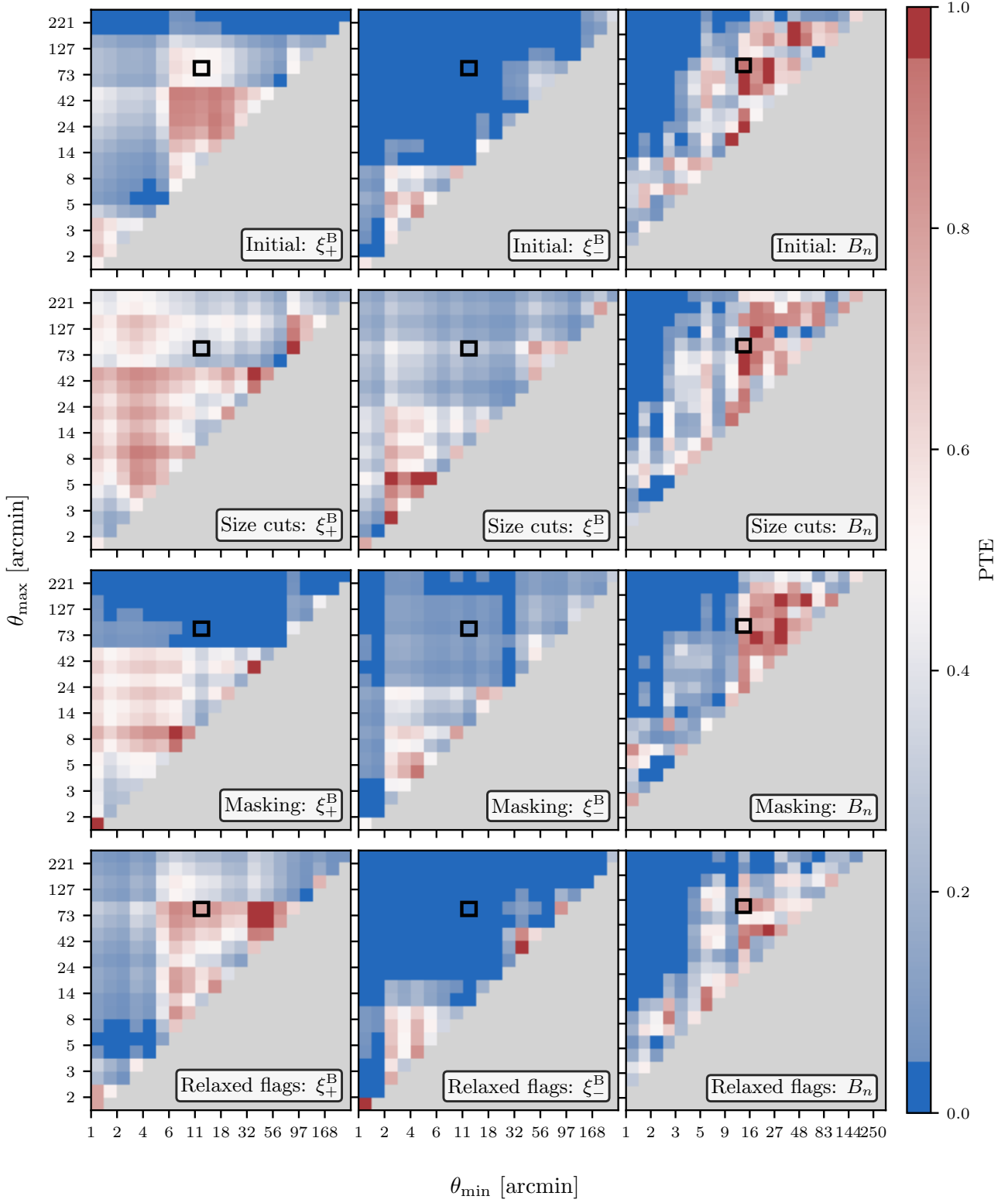


Fig. B.2: Configuration-space PTE maps for all four catalog versions (Paper I, Table 2). Columns show ξ_+^B , ξ_-^B , and COSEBI B_n PTEs as a function of angular scale cuts. Black squares mark the fiducial cuts; black contours demarcate PTE = 0.05.

References

- Abbott, T. M. C., Aguena, M., Alarcon, A., et al. 2022, Phys. Rev. D, 105, 023520
- Alonso, D., Sanchez, J., Slosar, A., & LSST Dark Energy Science Collaboration. 2019, MNRAS, 484, 4127
- Asgari, M. & Heymans, C. 2019, MNRAS, 484, L59
- Asgari, M., Heymans, C., Hildebrandt, H., et al. 2019, A&A, 624, A134
- Asgari, M., Lin, C.-A., Joachimi, B., et al. 2021, A&A, 645, A104
- Asgari, M., Schneider, P., & Simon, P. 2012, A&A, 542, A122
- Bacon, D. J., Refregier, A. R., & Ellis, R. S. 2000, MNRAS, 318, 625
- Blandford, R. D., Saust, A. B., Brainerd, T. G., & Villumsen, J. V. 1991, MNRAS, 251, 600
- Boulade, O., Charlot, X., Abbon, P., et al. 2003, in Society of Photo-Optical Instrumentation Engineers (SPIE) Conference Series, Vol. 4841, Instrument Design and Performance for Optical/Infrared Ground-based Telescopes, ed. M. Iye & A. F. M. Moorwood, 72–81
- Crittenden, R. G., Natarajan, P., Pen, U.-L., & Theuns, T. 2002, ApJ, 568, 20
- Dalal, R., Li, X., Nicola, A., et al. 2023, Phys. Rev. D, 108, 123519
- Fang, X., Eifler, T., & Krause, E. 2020, MNRAS, 497, 2699
- Farrrens, S., Guinot, A., Kilbinger, M., et al. 2022, A&A, 664, A141
- Gatti, M., Sheldon, E., Amon, A., et al. 2021, MNRAS, 504, 4312
- Goh, L. W. K. et al. 2025, in preparation
- Guerrini, S., Kilbinger, M., Leterme, H., et al. 2025, A&A, 700, A215
- Guerrini, S. et al. 2025, in preparation
- Guinot, A., Kilbinger, M., Farrrens, S., et al. 2022, A&A, 666, A162
- Gwyn, S., McConnachie, A. W., Cuillandre, J.-C., et al. 2025, arXiv e-prints, arXiv:2503.13783
- Hartlap, J., Simon, P., & Schneider, P. 2007, A&A, 464, 399
- Hervas Peters, F. et al. 2025a, in preparation
- Hervas Peters, F. et al. 2025b, in preparation
- Hilbert, S., Hartlap, J., White, S. D. M., & Schneider, P. 2009, A&A, 499, 31
- Huff, E. & Mandelbaum, R. 2017, arXiv e-prints, arXiv:1702.02600
- Jarvis, M., Bernstein, G., & Jain, B. 2004, MNRAS, 352, 338
- Jefferson, J., Omori, Y., Chang, C., et al. 2025, The Open Journal of Astrophysics, 8, 139
- Kaiser, N. 1992, ApJ, 388, 272
- Kaiser, N., Wilson, G., & Luppino, G. A. 2000, arXiv e-prints, astro
- Kamionkowski, M., Kosowsky, A., & Stebbins, A. 1997, Phys. Rev. D, 55, 7368
- Krause, E. & Eifler, T. 2017, MNRAS, 470, 2100
- Li, X., Zhang, T., Sugiyama, S., et al. 2023, Phys. Rev. D, 108, 123518
- Miralda-Escude, J. 1991, ApJ, 380, 1
- Planck Collaboration. 2020, A&A, 641, A6
- Reinecke, M. & Seljebotn, D. S. 2023, A&A, 678, A165
- Schneider, P. 1996, MNRAS, 283, 837
- Schneider, P., Asgari, M., Jozani, Y. N., et al. 2022, A&A, 664, A77
- Schneider, P., Eifler, T., & Krause, E. 2010, A&A, 520, A116
- Schneider, P., van Waerbeke, L., Jain, B., & Kruse, G. 1998, MNRAS, 296, 873
- Schneider, P., van Waerbeke, L., & Mellier, Y. 2002, A&A, 389, 729
- Sheldon, E. S. & Huff, E. M. 2017, ApJ, 841, 24
- Stebbins, A. 1996, arXiv e-prints, astro
- Tessore, N., Loureiro, A., Joachimi, B., von Wietersheim-Kramsta, M., & Jefrey, N. 2023, The Open Journal of Astrophysics, 6, 11
- Van Waerbeke, L., Mellier, Y., Erben, T., et al. 2000, A&A, 358, 30
- Wittman, D. M., Tyson, J. A., Kirkman, D., Dell'Antonio, I., & Bernstein, G. 2000, Nature, 405, 143
- Wolz, K., Alonso, D., & Nicola, A. 2025, J. Cosmology Astropart. Phys., 2025, 028
- Wright, A. H., Stölzner, B., Asgari, M., et al. 2025, arXiv e-prints, arXiv:2503.19441
- Zhang, T., Li, X., Dalal, R., et al. 2023, MNRAS, 525, 2441